

Dissipation and velocity distribution at the shear-driven jamming transition

Peter Olsson

Department of Physics, Umeå University, 901 87 Umeå, Sweden

(Received 10 August 2015; revised manuscript received 15 April 2016; published 28 April 2016)

We investigate energy dissipation and the distribution of particle velocities at the jamming transition for overdamped shear-driven frictionless disks in two dimensions at zero temperature. We find that the dissipation is caused by the fastest particles and that the fraction of particles responsible for the dissipation decreases towards zero as jamming is approached. These particles belong to an algebraic tail of the velocity distribution that approaches $\sim v^{-3}$ as jamming is approached. We further find that different measures of the velocity diverge differently, which means that concepts such as typical velocity may no longer be used, a finding that should have implications for analytical approaches to shear-driven jamming.

DOI: [10.1103/PhysRevE.93.042614](https://doi.org/10.1103/PhysRevE.93.042614)

I. INTRODUCTION

The hypothesis that the slowing down of the dynamics in systems as different as supercooled liquids, granular materials, colloids, foams, and emulsions, having a common origin in the properties of a critical point, point J [1], has inspired a great amount of work on jamming in the past decade. Several models have been used to try to pinpoint the properties of this jamming transition. Some of them have centered around a greatly simplified numerical model of spheres with contact-only interaction. One important branch has been to examine the properties of randomly generated static packings [2], whereas another has been to study the jamming transition through simulations of elastic particles under steady shear [3].

A key feature of jamming is the approach of the contact number z to the isostatic number z_{iso} , which is just enough for mechanical stability. It has recently been shown [4] that this is directly linked to the divergence of $\eta_p \equiv p/\dot{\gamma}$, the pressure equivalent of the shear viscosity. A related phenomenon is the increase in particle velocity as $\phi \rightarrow \phi_J$ [5,6]. This is related to the distribution of particle displacements due to a small shear increment that has been determined both in experiments of sheared granular materials [7] and in quasistatic simulations [5,7]. It was there found that this distribution is sufficiently wide that the non-Gaussian parameter $\langle \Delta y^4 \rangle / 3 \langle (\Delta y)^2 \rangle - 1$ diverges as ϕ_J is approached from below, granted that the shear step is sufficiently small.

In this paper we show that there is more to the particle velocity distribution than has so far been realized. Dissipation is mainly caused by the fastest particles and we find that the fraction of particles that are responsible for the dissipation decreases towards zero as jamming is approached. This behavior is related to an algebraic tail $P(v) \sim v^{-3}$ in the velocity distribution and we show that the velocity histograms determined at the jamming density approach this limiting behavior as $\dot{\gamma} \rightarrow 0$. Since rheology and dissipation are linked through power balance, the understanding of this phenomenon is right at the center of the phenomenon of shear-driven jamming. Furthermore, a close look at the velocity distribution shows that its behavior implies that different measures of the velocity behave differently, which should have a profound consequence for analytical approaches to jamming, since concepts such as typical velocity then become useless.

II. MODEL AND SIMULATIONS

Following O'Hern *et al.* [2], we use a simple model of bidisperse frictionless soft disks in two dimensions with equal numbers of disks with two different radii in the ratio 1.4. Length is measured in units of the diameter of the small particles d_s . We use Lees-Edwards boundary conditions [8] to introduce a time-dependent shear strain $\gamma = t\dot{\gamma}$. With periodic boundary conditions on the coordinates x_i and y_i in an $L \times L$ system, the position of particle i in a box with strain γ is defined as $\mathbf{r}_i = (x_i + \gamma y_i, y_i)$. The ordinary velocity is $\mathbf{v}_i^{\text{tot}} = \dot{\mathbf{r}}_i$, but in the following we consider the nonaffine velocity $\mathbf{v}_i = \mathbf{v}_i^{\text{tot}} - \mathbf{v}_R(\mathbf{r}_i)$, where $\mathbf{v}_R(\mathbf{r}_i) \equiv \dot{\gamma} y_i \hat{x}$ is a uniform shear velocity. With r_{ij} the distance between the centers of two particles and d_{ij} the sum of their radii, the relative overlap is $\delta_{ij} = 1 - r_{ij}/d_{ij}$ and the interaction between overlapping particles is $V(r_{ij}) = \epsilon \delta_{ij}^2 / 2$; we take $\epsilon = 1$. The force on particle i from particle j is $\mathbf{f}_{ij}^{\text{el}} = -\nabla_i V(r_{ij})$. The simulations are performed at zero temperature.

We consider two different models for the energy dissipation. In both cases the interaction force is $\mathbf{f}_i^{\text{el}} = \sum_j \mathbf{f}_{ij}^{\text{el}}$, where the sum extends over all particles j in contact with i and the equation of motion is

$$\mathbf{f}_i^{\text{el}} + \mathbf{f}_i^{\text{dis}} = m_i \ddot{\mathbf{r}}_i. \quad (1)$$

Most of our simulations have been done with the RD₀ (reservoir dissipation) model with the dissipating force

$$\mathbf{f}_{\text{RD},i}^{\text{dis}} = -k_d \mathbf{v}_i. \quad (2)$$

We take $k_d = 1$, $m_i = 0$, and the time unit $\tau_0 = d_s k_d / \epsilon$. We simulate $N = 65\,536$ particles with shear rates down to $\dot{\gamma} = 10^{-10}$. Checking for finite-size effects at $\dot{\gamma} = 10^{-9}$, we found no difference when using instead $N = 262\,144$. The equations of motion were integrated with the Heuns method with time step $\Delta t = 0.2\tau_0$.

Some additional simulations have also been done with the CD₀ (contact dissipation) model with dissipation due to velocity differences of disks in contact [3,9]. Details of these simulations may be found elsewhere [10].

III. RESULTS

A. Dissipation and the fastest particles

A key quantity in the present paper is the energy dissipation. We here just remark that this is a central quantity due to

the relation between dissipation and rheology from power balance $V\sigma\dot{\gamma} = k_d \langle \sum_i \mathbf{v}_i^2 \rangle$ [11] and we therefore believe that the considerations here may be instrumental in developing a better understanding of shear-driven jamming.

Our first key result is that most of the energy is dissipated by a small fraction of fast particles and, furthermore, that the fraction of particles needed to dissipate a given part of the power decreases as jamming is approached. Note that “fast” is here used in a relative sense. For low $\dot{\gamma}$ all particles are slow, it is only $v/\dot{\gamma}$ that can be big. To study the dissipation we introduce the velocity distribution function $P_v(v)$ such that $P_v(v)dv$ is the fraction of particles with velocity $v \leq |\mathbf{v}| < v + dv$. Figure 1(a) shows $P_v(v)$ vs $v/\dot{\gamma}$ both at five densities below ϕ_J and for three different shear rates at ϕ_J . (To get histograms of good quality down to small P_v we use bins that are equally spaced in $\ln v$.) The different simulation parameters $(\phi, \dot{\gamma})$ and their corresponding symbols are shown in the inset of Fig. 1(a). The points connected by solid lines and dashed lines, respectively, show two different ways to approach jamming. The solid line connects $(\phi, \dot{\gamma})$ at $\phi < \phi_J$ and at sufficiently low $\dot{\gamma}$ to be very close to the hard disk limit. The dashed line connects three points at $\phi = 0.8433 \approx \phi_J$. Here jamming is approached as $\dot{\gamma} \rightarrow 0$.

To study the dissipation with focus on the fast particles we define

$$x(v) = \int_v^\infty P_v(v') dv', \quad \bar{C}_2(v) = \int_v^\infty P_v(v') v'^2 dv' \quad (3)$$

such that $x(v)$ is the fraction of fast particles with $|\mathbf{v}| > v$ and $k_d \bar{C}_2(v)$ is the dissipating power due to the same particles. We also define $C_2(x) = \bar{C}_2(v(x))$, where $v(x)$ is the inverse of $x(v)$. Figure 1(b) shows the normalized C_2 vs x for the data in Fig. 1(a). The faster particles always dominate the dissipation, but this effect becomes more pronounced—the curves get steeper—as jamming is approached; a smaller fraction of particles is then needed for a given part of the dissipation. As a simple quantitative measure we introduce x_{50} , shown in the inset of Fig. 1(b), as the fraction of the fastest particles that dissipates 50% of the power. For the hard disk limit (solid line) x_{50} decreases as ϕ increases towards ϕ_J . The behavior of x_{50} at $\phi = 0.8433 \approx \phi_J$ is shown by the open squares in the inset of Fig. 1(c); x_{50} decreases with decreasing $\dot{\gamma}$ and gets as low as 0.16% at the lowest shear rate $\dot{\gamma} = 10^{-10}$. We believe that this localization of the dissipation to a few faster particles is related to plastic events or avalanches that are found above ϕ_J , as already speculated by others [5].

Figure 1(c) shows that the CD_0 model behaves similarly. In this model it is the velocity differences of contacting particles that is the quantity of interest rather than the nonaffine velocity, and C_2 is defined analogously. The main data in Fig. 1(c) are $C_2(x)$ at ϕ_J for the CD_0 model, which are very similar to the three data sets at ϕ_J in Fig. 1(a). As a more detailed comparison, the inset of Fig. 1(c) shows x_{50} against $\dot{\gamma}$ at ϕ_J for both the RD_0 model and the CD_0 model and it is clear that this fraction decreases with decreasing $\dot{\gamma}$ in both models. The effect studied here is thus not just peculiar to the simpler RD_0 model [12].

The evidence from Fig. 1 strongly suggests that $C_2(x)/C_2(1)$ approaches a step function as $\phi \rightarrow \phi_J$ and $\dot{\gamma} \rightarrow 0$ and this is the main result from the first part of this paper.

For $C_2(x)/C_2(1)$ to approach a step function the limiting distribution has to have a tail

$$P_v(v) \sim v^{-3}, \quad (4)$$

since that would make $C_2(v)$ diverge. We note that experiments on dense granular flows have led to similar conclusions [13]. Before turning to more elaborate analyses, we note that the dashed line in Fig. 1(a) with slope equal to -3 gives some support for Eq. (4) as the limiting behavior at ϕ_J as $\dot{\gamma} \rightarrow 0$.

For the further analysis it is important to understand the origin of the wide distribution. We note that the nonaffine velocity in the RD_0 model is related to the sum of all (repulsive)

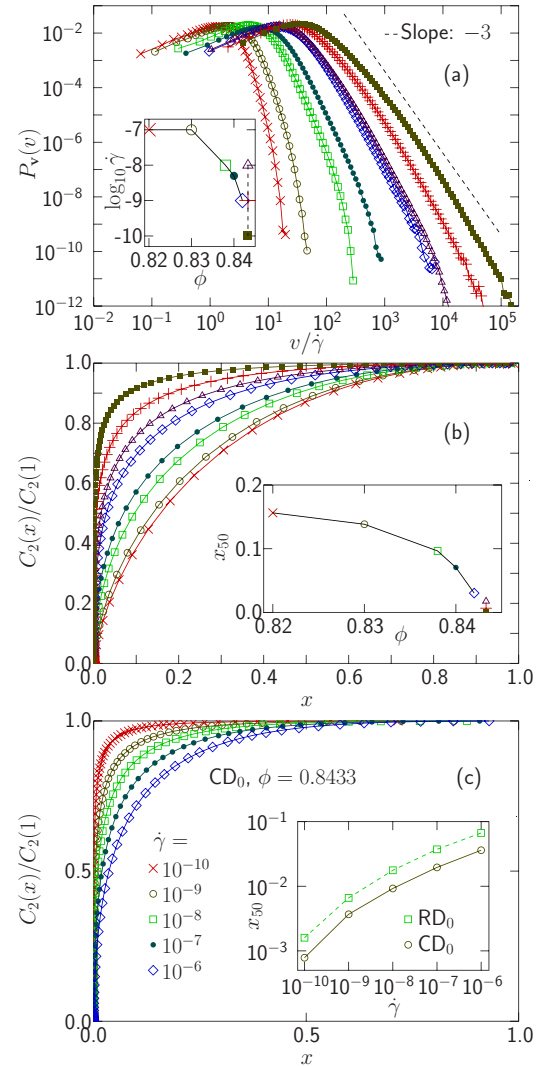


FIG. 1. Velocity distribution and dissipation. (a) Velocity distribution function $P_v(v)$ vs $v/\dot{\gamma}$ with simulation parameters $(\phi, \dot{\gamma})$ and symbols as shown in the inset. The dashed line has slope -3 . (b) Part of the dissipated power that is dissipated by the fraction x of the fastest particles. (c) Same quantity for the CD_0 model. These data are at $\phi = 0.8433 \approx \phi_J$ and five different shear rates. The insets of (b) and (c) are x_{50} , the fraction of particles needed to dissipate 50% of the power. The inset of (b) shows that x_{50} for the RD_0 model decreases as ϕ increases, whereas the inset of (c) shows x_{50} at ϕ_J decreasing with $\dot{\gamma}$ for both RD_0 and CD_0 .

contact forces that act on the particle. The nonaffine velocity of particle i is $\mathbf{v}_i = \sum_j \mathbf{f}_{ij}^{\text{el}}/k_d$. Close to jamming, the forces on most particles almost cancel one another out and the total force is typically very small compared to the average force, $f_i^{\text{el}} \ll f_{ij}^{\text{el}}$, as has also been noted by others [14]. There are, however, some particles for which the forces do not balance one another out and the velocity of these particles can then be much larger than the average velocity. The wide distribution is thus due to the big difference between the individual forces and the typical total force.

A consequence of this picture is that the maximum velocity is bounded by the typical f_{ij}^{el} , which means that the possibly algebraic distribution is cut off by an exponential factor e^{-v/v_c} , where $v_c \sim f_{ij}^{\text{el}}/k_d \sim p/k_d d_s$. (This also suggests $v_c/\dot{\gamma} \sim \eta_p$.) This behavior is seen in Fig. 1(a) as the approximately rectilinear (i.e., algebraic) behaviors for intermediate values of $P_v(v)$ turn into more rapid decays at higher velocities. One therefore expects the tails in the distributions to be described by $P(v) \sim v^{-r} e^{-v/v_c}$ and this exponential decay becomes a complicating factor when one attempts to determine r from $P(v)$.

B. Different measures of the velocity

Our second key result is that different measures of the velocity behave differently. This is important since it means that concepts such as typical velocity, used in various theoretical approaches, become useless. Figure 2 shows simulation results

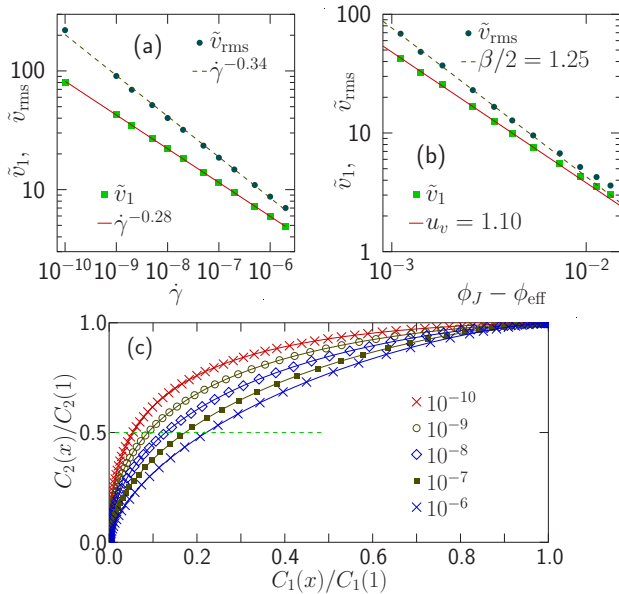


FIG. 2. Two different measures of the velocity: \tilde{v}_{rms} and \tilde{v}_1 for (a) $\phi = 0.8433 \approx \phi_J$ vs $\dot{\gamma}$ and (b) data below ϕ_J plotted vs distance to jamming; only the points with $\phi_J - \phi_{\text{eff}} < 0.006$ were used for the fits. Here ϕ_{eff} is the effective density. The lines are $\sim (\phi_J - \phi_{\text{eff}})^{-u_v}$ and $\sim (\phi_J - \phi_{\text{eff}})^{-\beta/2}$. (c) Plot connects back to Fig. 1(a) but is C_2 , related to \tilde{v}_{rms}^2 , against C_1 , which is related to \tilde{v}_1 . From the crossings of the dashed line one may read off the relative contribution to \tilde{v}_1 from the fraction of the fastest particles that dissipate 50% of the energy, a quantity that decreases with decreasing $\dot{\gamma}$.

for \tilde{v}_1 and \tilde{v}_{rms} , defined through

$$\tilde{v}_1 = \langle |\tilde{\mathbf{v}}| \rangle, \quad \tilde{v}_{\text{rms}}^2 = \langle \tilde{\mathbf{v}}^2 \rangle, \quad (5)$$

with the notation $\tilde{\mathbf{v}} = \mathbf{v}/\dot{\gamma}$. In Fig. 2(a) these quantities are plotted against $\dot{\gamma}$ and are found to diverge algebraically with different exponents: $\tilde{v}_{\text{rms}} \sim \dot{\gamma}^{-\beta/2z\nu} \sim \dot{\gamma}^{-0.34}$ and $\tilde{v}_1 \sim \dot{\gamma}^{-u_v/z\nu} \sim \dot{\gamma}^{-0.28}$. [The expressions follow by taking $b = \dot{\gamma}^{-1/z}$ in $\mathcal{O}(\phi, \dot{\gamma}) = b^{u_\phi/v} g_\phi((\phi_J - \phi)b^{1/v}, \dot{\gamma}b^z)$ [15] with the scaling dimension u_ϕ equal to u_v for \tilde{v}_1 and $\beta/2$ for \tilde{v}_{rms} . The latter follows from $\eta \sim \tilde{v}_{\text{rms}}^2$ and $\eta(\phi, \dot{\gamma} \rightarrow 0) \sim (\phi_J - \phi)^{-\beta}$.]

It is instructive to also examine the same quantities with data below ϕ_J , close to the hard disk limit. The starting point is the relations for hard disks $\tilde{v}_1^{\text{HD}}(\phi) \sim (\phi_J - \phi)^{-u_v}$ and $\tilde{v}_{\text{rms}}^{\text{HD}}(\phi) \sim (\phi_J - \phi)^{-\beta/2}$ that follow by using $b = \dot{\gamma}$ in the scaling expressions and considering $\dot{\gamma} \rightarrow 0$. In Fig. 2(b) we make use of the effective-density mapping of soft disks onto hard disks $\mathcal{O}^{\text{HD}}(\phi_{\text{eff}}) = \mathcal{O}(\phi, \dot{\gamma})$, where the effective density is $\phi_{\text{eff}} = \phi - cE^{1/2y}$, with $c = 1.53$ and $y = 1.09$, as detailed in Ref. [16]. Figure 2(b) shows \tilde{v}_1 and \tilde{v}_{rms} against $\phi_J - \phi_{\text{eff}}$. The solid line gives the exponent $u_v = 1.10$ in agreement with $\ell_\Delta \sim (\phi_J - \phi)^{-1.1}$ for the particle velocity in Ref. [5]. The dashed line gives $\beta/2 = 1.25$. (The value $\beta = 2.50$ is somewhat low in comparison to recent estimates [15], but this could be due to not including corrections to scaling [15].) Note that the exponents from Figs. 2(a) and 2(b) are consistent when using $1/z\nu = 0.26$ [15].

The reason for the different behaviors of \tilde{v}_1 and \tilde{v}_{rms} is that the dominant contribution to these quantities comes from different velocity intervals. This is illustrated in Fig. 2(c), which shows how $C_2(x)$ in Eq. (3) and $C_1(x)$ (for v^1 instead of v^2) increase to their respective limits $C_2(1) = \tilde{v}_{\text{rms}}^2$ and $C_1(1) = \tilde{v}_1$, as x (the fraction of the fastest particles included in the calculations) increases. The different curves get steeper for smaller $\dot{\gamma}$ and for $\dot{\gamma} = 10^{-10}$ we find $C_1(x) \approx 0.05$ when $C_2(x) = 0.5$, which thus shows that \tilde{v}_{rms}^2 gets a considerably larger contribution from the highest velocity part of the histogram than \tilde{v}_1 . An extrapolation of these curves to the $\dot{\gamma} \rightarrow 0$ limit would give a step function (though this is not as clear as in Fig. 1), which would imply that \tilde{v}_{rms}^2 and \tilde{v}_1 were controlled by different velocity intervals and that there would be no reason for these quantities to be at all related.

C. Analysis of the velocity distribution function

We will now relate our two key results of Figs. 1 and 2 to properties of the velocity distribution function with the goals (i) to examine how the exponent in Eq. (4) approaches -3 as $\dot{\gamma} \rightarrow 0$ (this exponent will be denoted by $-r$) and (ii) to shed some more light on the mechanism that allows \tilde{v}_1 and \tilde{v}_{rms} to diverge differently. We have then found it convenient to use $P(\tilde{v}_y)$, the distribution of the absolute value of the y component. This quantity differs from P_v in that it approaches a constant at small velocities, which is a feature that makes it easier to find an analytical expression that fits the data. Figure 3(a) shows $P(\tilde{v}_y)$ for several different $\dot{\gamma}$ at $\phi = 0.8433 \approx \phi_J$ together with solid lines that are fits to the expression

$$P(\tilde{v}_y) = \frac{A e^{-\tilde{v}_y/\tilde{v}_c}}{1 + (\tilde{v}_y/\tilde{v}_a)^2 + (\tilde{v}_y/\tilde{v}_s)^r}, \quad (6)$$

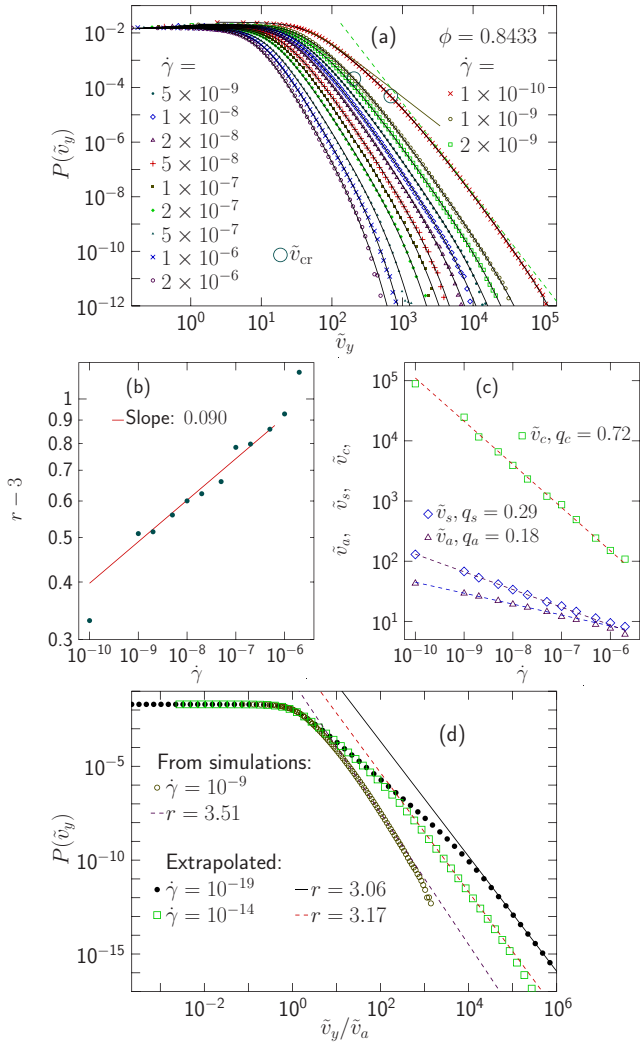


FIG. 3. Velocity distribution and fitting parameters for different $\dot{\gamma}$ at $\phi = 0.8433 \approx \phi_J$. (a) Velocity distribution $P(\tilde{v}_y)$. (b) Plot of $r - 3$ vs $\dot{\gamma}$ from fitting to Eq. (6). Fitting $r - 3 \sim \dot{\gamma}^{q_r}$ for $10^{-9} \leq \dot{\gamma} \leq 5 \times 10^{-7}$ gives $q_r = 0.09 \pm 0.02$. (c) Shear rate dependence of the velocity scales in Eq. (6). (d) Plot arguing that there is no limiting velocity distribution function by showing the measured $P(\tilde{v}_y)$ for $\dot{\gamma} = 10^{-9}$ together with extrapolated $P(\tilde{v}_y)$ for two even lower shear rates $\dot{\gamma} = 10^{-14}$ and 10^{-19} .

with A , \tilde{v}_c , \tilde{v}_a , \tilde{v}_s , and r as free parameters. This expression crosses over from a constant at small \tilde{v}_y to a large- \tilde{v}_y tail with $\tilde{v}_y^{-r} e^{-\tilde{v}_y/\tilde{v}_c}$ (as discussed above) and the crossover is governed by an additional term in the denominator, $(\tilde{v}_y/\tilde{v}_a)^a$. For best possible fits, a should be an additional free parameter, but since a anyway tends to be close to 2 and $a = 2$ opens up for analytical calculations, we here fix $a = 2$. Figure 3(b) shows the exponent of the algebraic tail as $r - 3$ vs $\dot{\gamma}$. The rectilinear behavior suggests that r decays algebraically to 3, consistent with the limiting behavior of Eq. (4), as $r - 3 \sim \dot{\gamma}^{q_r}$ with $q_r = 0.09 \pm 0.02$. Figure 3(c) shows the three different velocity scales in Eq. (6) and their dependences on $\dot{\gamma}$: $\tilde{v}_a \sim \dot{\gamma}^{-q_a}$, $\tilde{v}_s \sim \dot{\gamma}^{-q_s}$, and $\tilde{v}_c \sim \dot{\gamma}^{-q_c}$, with the exponents $q_a = 0.18$, $q_s = 0.29$, and $q_c = 0.72$. The Appendix shows analytical calculations of \tilde{v}_1 and \tilde{v}_{rms} based on these $\dot{\gamma}$ dependences together with an approximation of Eq. (6).

The common belief that \tilde{v}_1 and \tilde{v}_{rms} would diverge in the same way is related to the expectation of a limiting velocity distribution function as $\dot{\gamma} \rightarrow 0$. We therefore stress that a consequence of the differing behaviors of \tilde{v}_a and \tilde{v}_s is a velocity distribution function that keeps changing with $\dot{\gamma}$ and never approaches any limiting function. To illustrate how this could happen, we will show some extrapolated data for very small $\dot{\gamma}$, even though such extrapolations can never be entirely reliable. Figure 3(d) thus shows the measured $P(\tilde{v}_y)$ vs \tilde{v}_y/\tilde{v}_a for $\dot{\gamma} = 10^{-9}$ together with two data sets calculated for $\dot{\gamma} = 10^{-14}$ and 10^{-19} from Eq. (6), by extrapolating the parameters in this equation according to the fitting lines in Figs. 3(b) and 3(c). The straight lines in Fig. 3(d) are $\sim \tilde{v}_y^{-r}$ with different r and we see that the data cross over from $A/[1 + (\tilde{v}_y/\tilde{v}_a)^2]$ to these respective algebraic behaviors, at larger \tilde{v}_y/\tilde{v}_a , as $\dot{\gamma}$ decreases. Since a large amount of the dissipation takes place in the algebraic tail, this tail can never be neglected and we thus conclude that there is in effect no limiting velocity distribution function.

We now turn to the crossover velocity $\tilde{v}_{\text{cr}} = (\tilde{v}_s^r/\tilde{v}_a^2)^{1/(r-2)}$ that describes the crossover from exponent -2 to exponent $-r$, which is obtained by equating the two velocity-dependent terms in the denominator of Eq. (6). This quantity is shown by the big open circles in Fig. 3(a), which are $P(\tilde{v}_{\text{cr}})$ vs \tilde{v}_{cr} for $\dot{\gamma} = 10^{-9}$ and 10^{-10} . These are the last two points in a persistent trend to smaller $P(\tilde{v}_{\text{cr}})$, which shows that the fraction of particles in the algebraic tail decreases with $\dot{\gamma}$. This also echoes the conclusion from Fig. 1 that the fraction of particles that are responsible for the dissipation decreases with $\dot{\gamma}$.

The connection between the algebraic tail and the dissipation is made more direct by Fig. 4(a), which shows that \tilde{v}_{cr} and \tilde{v}_{50} behave essentially the same. Here \tilde{v}_{50} , related to x_{50} above, is the velocity above which 50% of the dissipation takes place and we may therefore conclude that the particles in the tail are responsible for well above 50% of the dissipation.

From Fig. 4(a) we may also conclude that the size of this algebraic tail increases with decreasing $\dot{\gamma}$. Since \tilde{v}_{cr} and \tilde{v}_c

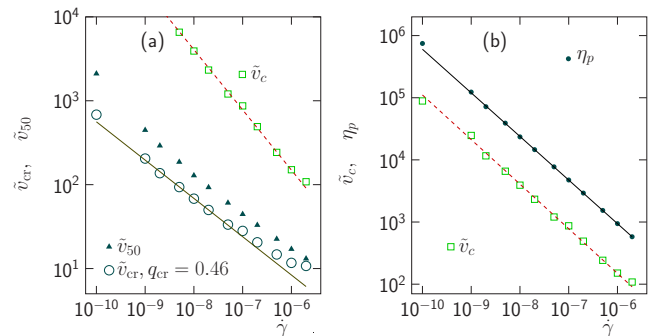


FIG. 4. Comparison of different velocity scales. (a) Plot of \tilde{v}_{cr} , which is the velocity scale for the crossover to the algebraic tail $\sim \tilde{v}_y^{-r}$, together with \tilde{v}_{50} , which is the velocity above which 50% of the dissipation takes place, and the cutoff velocity \tilde{v}_c . The similar behaviors of \tilde{v}_{cr} and \tilde{v}_{50} show that a large part of the dissipation occurs in the algebraic tail and the increasing distance between \tilde{v}_c and \tilde{v}_{cr} shows that this tail becomes wider as $\dot{\gamma} \rightarrow 0$. (b) Plot confirming the expectation that the pressure (note that $\eta_p \equiv p/\dot{\gamma}$) and the cutoff velocity are directly related.

mark the onset and the end of this tail, the increasing distance between these points (open circles and open squares) means that the size of the algebraic region increases as $\dot{\gamma} \rightarrow 0$. We thus find that this tail widens even though it involves a smaller number of particles as $\dot{\gamma}$ decreases.

It is also interesting to note that \tilde{v}_c and η_p in Fig. 4(b) behave essentially the same. This is also in agreement with the above discussion of the origin of the wide distribution, where we argued that the maximum velocity has to be bounded by the typical force in the system, which in turn is related to the pressure. We also finally remark that the combination of an algebraic decay and an exponential cutoff makes it difficult to get good precision in the determination of the exponent for the decay. This effect is most problematic at the lowest shear rate $\dot{\gamma} = 10^{-10}$ and this point was therefore not included in the above determination of q_r . The difficulty to determine r with good precision is related to the covariation of r and \tilde{v}_c , which is seen in Figs. 3(b) and 3(c). The reason for this effect is that a small decrease in r can be compensated by a small decrease in \tilde{v}_c since a smaller r gives a slower decay, while a smaller \tilde{v}_c gives a faster decay.

IV. SUMMARY

To summarize, we have found that the fraction of particles that are responsible for the energy dissipation decreases towards zero as jamming is approached. These particles belong to a tail in the velocity distribution that approaches $P(v) \sim v^{-3}$ at jamming. We further found that different measures of the velocity diverge differently, which means that concepts such as typical velocity no longer appear to be useful. We have demonstrated this by arguing in Fig. 2(c) that \tilde{v}_1 and \tilde{v}_{rms} get their contributions from different parts of the velocity histogram, by demonstrating that the shape of the velocity distribution keeps changing when $\dot{\gamma}$ decreases, without approaching any limiting velocity distribution, and finally with analytical calculations in the Appendix.

ACKNOWLEDGMENTS

I thank S. Teitel for many illuminating discussions. This work was supported by the Swedish Research Council Grant No. 2010-3725. Simulations were performed on resources provided by the Swedish National Infrastructure for Computing at PDC and HPC2N.

APPENDIX: ANALYTICAL CALCULATIONS

The purpose of the calculations below is to illustrate the mechanism that gives different behaviors for \tilde{v}_1 and \tilde{v}_{rms} . The idea is here to split the expression for the velocity distribution (6) into three different parts

$$P(\tilde{v}_y) \sim \begin{cases} 1/[1 + (\tilde{v}_y/\tilde{v}_a)^2], & 0 \leq \tilde{v}_y < \tilde{v}_{\text{cr}} \\ 1/(\tilde{v}_y/\tilde{v}_s)^r, & \tilde{v}_{\text{cr}} < \tilde{v}_y < \tilde{v}_c \\ 0, & \tilde{v}_c < \tilde{v}_y. \end{cases} \quad (\text{A1})$$

We may then determine $\tilde{v}_1 = \langle \tilde{v}_y \rangle$ and $\tilde{v}_{\text{rms}}^2 = \langle \tilde{v}_y^2 \rangle$ by calculating some integrals analytically.

To determine $\tilde{v}_1 = \langle \tilde{v}_y \rangle$ and $\tilde{v}_{\text{rms}}^2 = \langle \tilde{v}_y^2 \rangle$ we need the integrals I_0 , I_1 , and I_2 ,

$$I_p = \int P(\tilde{v}_y) \tilde{v}_y^p d\tilde{v}_y,$$

which with Eq. (A1) becomes

$$I_p = \int_0^{\tilde{v}_{\text{cr}}} \frac{\tilde{v}_y^p}{1 + (\tilde{v}_y/\tilde{v}_a)^2} d\tilde{v}_y + \int_{\tilde{v}_{\text{cr}}}^{\tilde{v}_c} \tilde{v}_y^p (\tilde{v}_y/\tilde{v}_s)^{-r} d\tilde{v}_y.$$

It is then convenient to consider the two terms above separately.

1. First term $I_p^{(1)}$

We here use $x = \tilde{v}_y/\tilde{v}_a$, $dx = d\tilde{v}_y/\tilde{v}_a$, and $x_{\text{cr}} = \tilde{v}_{\text{cr}}/\tilde{v}_a$ and handle the different integrals separately for different p : For $p = 0$,

$$\begin{aligned} I_0^{(1)} &= \tilde{v}_a \int_0^{x_{\text{cr}}} \frac{1}{1+x^2} dx = \tilde{v}_a [\arctan x]_0^{x_{\text{cr}}} \\ &= \tilde{v}_a \arctan(\tilde{v}_{\text{cr}}/\tilde{v}_a); \end{aligned} \quad (\text{A2})$$

for $p = 1$,

$$\begin{aligned} I_1^{(1)} &= \tilde{v}_a^2 \int_0^{x_{\text{cr}}} \frac{x}{1+x^2} dx = \tilde{v}_a^2 \left[\frac{1}{2} \ln(1+x^2) \right]_0^{x_{\text{cr}}} \\ &= \frac{\tilde{v}_a^2}{2} \ln[1 + (\tilde{v}_{\text{cr}}/\tilde{v}_a)^2]; \end{aligned} \quad (\text{A3})$$

and for $p = 2$,

$$\begin{aligned} I_2^{(1)} &= \tilde{v}_a^3 \int_0^{x_{\text{cr}}} \frac{x^2}{1+x^2} dx = \tilde{v}_a^3 [x - \arctan x]_0^{x_{\text{cr}}} \\ &= \tilde{v}_a^2 \tilde{v}_{\text{cr}} - \tilde{v}_a^3 \arctan(\tilde{v}_{\text{cr}}/\tilde{v}_a). \end{aligned} \quad (\text{A4})$$

2. Second term $I_p^{(2)}$

We here get an expression for general p :

$$\begin{aligned} I_p^{(2)} &= \tilde{v}_s^r \left[\frac{\tilde{v}_y^{p+1-r}}{p+1-r} \right]_{\tilde{v}_{\text{cr}}}^{\tilde{v}_c} \\ &= \frac{\tilde{v}_s^r}{p+1-r} (\tilde{v}_c^{p+1-r} - \tilde{v}_{\text{cr}}^{p+1-r}) \\ &= \frac{\tilde{v}_s^{p+1}}{r-1-p} \left[\left(\frac{\tilde{v}_s}{\tilde{v}_{\text{cr}}} \right)^{r-1-p} - \left(\frac{\tilde{v}_s}{\tilde{v}_c} \right)^{r-1-p} \right]. \end{aligned}$$

This splits into two cases. If $r-1-p \gg 0$ (which is always the case in our simulations) and $\tilde{v}_c \gg \tilde{v}_{\text{cr}}$ (which allows us to skip the second term) we make use of $\tilde{v}_{\text{cr}}^{r-2} = \tilde{v}_s^r/\tilde{v}_a^2$ to get

$$I_p^{(2)} \approx \frac{\tilde{v}_s^{p+1}}{r-1-p} \left(\frac{\tilde{v}_s}{\tilde{v}_{\text{cr}}} \right)^{r-1-p} = \frac{\tilde{v}_a^2 \tilde{v}_{\text{cr}}^{p-1}}{r-1-p}. \quad (\text{A5})$$

For $r - 1 - p \approx 0$, on the other hand, (possible for $p = 2$ and very close to jamming, $r \rightarrow 3$), we get

$$I_p^{(2)} \approx \tilde{v}_s^{p+1} \left[\ln \left(\frac{\tilde{v}_s}{\tilde{v}_{cr}} \right) - \ln \left(\frac{\tilde{v}_c}{\tilde{v}_a} \right) \right] = \tilde{v}_s^{p+1} \ln \left(\frac{\tilde{v}_c}{\tilde{v}_{cr}} \right). \quad (\text{A6})$$

3. Both terms together $I_p^{(1)} + I_p^{(2)}$

The normalization becomes

$$I_0 = \tilde{v}_a \arctan \left(\frac{\tilde{v}_{cr}}{\tilde{v}_a} \right) + \frac{1}{r-1} \frac{\tilde{v}_a^2}{\tilde{v}_{cr}} \approx \frac{\pi}{2} \tilde{v}_a, \quad (\text{A7})$$

where we skip the second term since $\tilde{v}_a/\tilde{v}_{cr} \ll 1$. For the first moment we get

$$I_1 = \frac{\tilde{v}_a^2}{2} \ln \left[1 + \left(\frac{\tilde{v}_{cr}}{\tilde{v}_a} \right)^2 \right] + \frac{\tilde{v}_a^2}{r-2} \approx \tilde{v}_a^2 \left[\ln \left(\frac{\tilde{v}_{cr}}{\tilde{v}_a} \right) + \frac{1}{r-2} \right]. \quad (\text{A8})$$

The logarithmic term may be written $\ln(\tilde{v}_{cr}/\tilde{v}_a) = \ln(\dot{\gamma}^{-q_{cr}}/\dot{\gamma}^{-q_a}) \sim (q_{cr} - q_a) \ln(1/\dot{\gamma})$, and using $q_a \approx 0.18$ and $q_{cr} \approx 0.46$, the average velocity becomes

$$\begin{aligned} \tilde{v}_1 = \langle \tilde{v}_y \rangle &= I_1/I_0 \approx \tilde{v}_a \left[\ln \left(\frac{\tilde{v}_{cr}}{\tilde{v}_a} \right) + \frac{1}{r-2} \right] \\ &\approx \tilde{v}_a \left[0.62 \log_{10}(1/\dot{\gamma}) + \frac{1}{r-2} \right]. \end{aligned} \quad (\text{A9})$$

For the second moment, for r not too close to 3, Eqs. (A4) and (A5) lead to

$$I_2 = \tilde{v}_a^2 \tilde{v}_{cr} \left[1 + \frac{1}{r-3} \right] - \tilde{v}_a^3 \arctan \left(\frac{\tilde{v}_{cr}}{\tilde{v}_a} \right) \quad (\text{A10})$$

and since $\arctan x < \pi/2$, the second term may be neglected and we get

$$\tilde{v}_{rms}^2 = \langle \tilde{v}_y^2 \rangle \approx \tilde{v}_a \tilde{v}_{cr} \left[1 + \frac{1}{r-3} \right], \quad (\text{A11})$$

For the second moment, with $r \rightarrow 3$, we instead use Eq. (A6), which gives (with $\tilde{v}_{cr} \approx \tilde{v}_s^3/\tilde{v}_a^2$ and $q_c = 0.71$)

$$\begin{aligned} \tilde{v}_{rms}^2 &= \langle \tilde{v}_y^2 \rangle \approx \tilde{v}_a \tilde{v}_{cr} + \frac{\tilde{v}_s^3}{\tilde{v}_a} \ln \left(\frac{\tilde{v}_c}{\tilde{v}_{cr}} \right) \\ &\approx \tilde{v}_a \tilde{v}_{cr} [1 + 0.58 \log_{10}(1/\dot{\gamma})] \end{aligned} \quad (\text{A12})$$

and shows that the effect of the cutoff \tilde{v}_c is to replace the divergence $\sim 1/(r-3)$ in Eq. (A11) with a slow logarithmic increase.

4. Small- $\dot{\gamma}$ limit

From Eq. (A12) the leading small- $\dot{\gamma}$ behavior for \tilde{v}_{rms} becomes $\tilde{v}_{rms}^2 \sim \tilde{v}_a \tilde{v}_{cr} \sim \dot{\gamma}^{-(q_{cr}+q_a)/2} \sim \dot{\gamma}^{-0.64}$, in very good agreement with $\tilde{v}_{rms} \sim \dot{\gamma}^{-0.34}$ in Fig. 2(a). For \tilde{v}_1 , the full expression in Eq. (A9) reproduces the exponent -0.28 in Fig. 2(a) for the same range of $\dot{\gamma}$. In the $\dot{\gamma} \rightarrow 0$ limit, however, the second term may be neglected and the slowly changing logarithm may be replaced by a constant. This gives $\tilde{v}_1 \sim \tilde{v}_a \sim \dot{\gamma}^{-q_a} \sim \dot{\gamma}^{-0.18}$, which is clearly different from the measured exponent -0.28 . We do however consider the exponent obtained directly from the measured data to be more reliable since it is from an excellent fit to data across four orders of magnitude in $\dot{\gamma}$. We note that \tilde{v}_1 is more sensitive than \tilde{v}_{rms} to the (questionable) approximation of $P(\tilde{v}_y)$ at intermediate velocities, between \tilde{v}_a and \tilde{v}_{cr} . This may be the reason why the present approach based on Eq. (A1) appears to fail for \tilde{v}_1 even though it works very well for \tilde{v}_{rms} . For $\dot{\gamma} = 10^{-19}$ in Fig. 3(d) this could mean that the true behavior is a smoother and more gradual curve than the (somewhat unrealistic) behavior with three distinct regions with $P(\tilde{v}_y) = \text{const}$, $P(\tilde{v}_y) \sim \tilde{v}_y^{-2}$, and $P(\tilde{v}_y) \sim \tilde{v}_y^{-3.06}$.

-
- [1] A. J. Liu and S. R. Nagel, *Nature (London)* **396**, 21 (1998).
[2] C. S. O'Hern, L. E. Silbert, A. J. Liu, and S. R. Nagel, *Phys. Rev. E* **68**, 011306 (2003).
[3] D. J. Durian, *Phys. Rev. Lett.* **75**, 4780 (1995).
[4] E. Lerner, G. Düring, and M. Wyart, *Proc. Natl. Acad. Sci. USA* **109**, 4798 (2012).
[5] C. Heussinger, L. Berthier, and J.-L. Barrat, *Europhys. Lett.* **90**, 20005 (2010).
[6] B. Andreotti, J.-L. Barrat, and C. Heussinger, *Phys. Rev. Lett.* **109**, 105901 (2012).
[7] G. Marty and O. Dauchot, *Phys. Rev. Lett.* **94**, 015701 (2005).
[8] D. J. Evans and G. P. Morriss, *Statistical Mechanics of Nonequilibrium Liquids* (Academic, London, 1990).
[9] B. P. Tighe, E. Woldhuis, J. J. C. Remmers, W. van Saarloos, and M. van Hecke, *Phys. Rev. Lett.* **105**, 088303 (2010).
[10] D. Vågberg, P. Olsson, and S. Teitel, *Phys. Rev. Lett.* **113**, 148002 (2014).
[11] I. K. Ono, S. Tewari, S. A. Langer, and A. J. Liu, *Phys. Rev. E* **67**, 061503 (2003).
[12] Preliminary analyses of data from three-dimensional systems suggest that they behave qualitatively the same. D. Vågberg and P. Olsson (unpublished).
[13] S. Moka and P. R. Nott, *Phys. Rev. Lett.* **95**, 068003 (2005).
[14] E. DeGiuli, G. Düring, E. Lerner, and M. Wyart, *Phys. Rev. E* **91**, 062206 (2015).
[15] P. Olsson and S. Teitel, *Phys. Rev. E* **83**, 030302(R) (2011).
[16] P. Olsson and S. Teitel, *Phys. Rev. Lett.* **109**, 108001 (2012).